SSRG International Journal of Electrical and Electronics Engineering
ISSN: 2348-8379/ https://doi.org/10.14445/23488379/IJEEE-V12I8P120

Volume 12 Issue 8, 226-245, August 2025

Original Article

A High-Efficiency PV-Based Charging System for Electric Vehicles Using Optimized MPPT and High-Gain Boost-Zeta Converter

J. Viswanatha Rao[1], S. Vijaya Madhavi[2], K. Kalaiyarasan[3], D. Sowmiya[4]

[1]*Department of Electrical and Electronics Engineering, VNR Vignana Jyothi Institute of Engineering and Technology, Hyderabad, Telangana, India.*
[2]*Department of Electrical and Electronics Engineering, Mallareddy Engineering College for Women (Autonomous), Hyderabad, Telangana, India.*
[3,4]*Faculty of Electrical Engineering, Anna University, Chennai, Tamilnadu, India.*

[1]*Corresponding Author : viswanath72@gmail.com*

Received: 15 June 2025 Revised: 16 July 2025 Accepted: 15 August 2025 Published: 30 August 2025

Abstract *- The increase in adoption of Electric Vehicles (EVs) continues to progress, owing to the pressing need for charging infrastructure that integrates Renewable Energy Sources (RESs), while maintaining eco-friendly standards. This research develops a Photovoltaic (PV) based EV charging system, reducing dependency on the grid and lowering the carbon footprint associated with conventional charging systems. The research incorporates a novel High Gain Boost-Zeta (HGBZ) converter to boost low PV voltage to a required level for EV charging, offering efficient transfer of energy. In addition, the Improved Coot Optimized Artificial Neural Network (ICO-ANN) Maximum Power Point Tracking (MPPT) algorithm is integrated to maximize power extraction from PV under changing sunlight conditions, ensuring consistent and reliable charging. The system also incorporates a Bidirectional DC-DC converter interfacing with an energy storage unit, allowing it to store excess solar energy when generation exceeds demand and supply power to EV during low solar production periods. The bidirectional capability ensures uninterrupted charging and improves the system, making it ideal for an EV charging station. A three-phase voltage source inverter (VSI) is incorporated into the grid connection, and EV charging is used to support flexible energy management. The system distributes excess solar energy to the grid or draws from it when additional power is needed, providing dynamic interaction with the grid and contributing to grid stability. The proposed system is analyzed using MATLAB, and the attained results are compared with state-of-the-art methodologies, revealing improved converter efficiency of 95.33% and tracking efficiency of 98.99%, thereby highlighting the effectiveness of the proposed work.*

Keywords *- PV System, HGBZ Converter, ICO-ANN MPPT, EV System, BLDC Motor, Battery, Grid Synchronization.*

1. Introduction

The steady rise in carbon emissions and decline in fossil fuel supply have encouraged the adoption of RESs [1], notably in the transportation sector. EVs have emerged as a favourable alternative to traditional combustion engine vehicles, offering solutions to minimize greenhouse gas emissions and reliance on fuels [2]. Among renewable sources, PV [1] is increasingly being incorporated into EV charging infrastructure, promoting a greener mode of transportation. Because of their power density, superior efficiency, low maintenance requirements, extended service life, fewer Electromagnetic Interference (EMI) problems, and small size, BLDC motors are frequently chosen over conventional DC motors in EVs. Table 1 provides a comprehensie review of various motors utilized in EVs. These features made BLDC motors the preferred choice for EV applications over the past decade. Additionally, the use of BLDC motors [7] helps optimize the size and cost of the EV's energy storage and power management systems.

Through the use of a DC-DC converter, solar panels are integrated with BLDC motor-driven systems to enhance the efficiency and performance of EVs. Traditional converters, including Boost, Buck-Boost, Cuk, and Single-Ended Primary Inductance Converter (SEPIC), are frequently used in EV applications to manage power regulation from PV. Nevertheless, Boost and Buck-boost converters [8] experience reduced efficiency under heavy load conditions. The Cuk [9] converter provides input-output isolation but adds complexity, whereas SEPIC [10], though versatile, suffers from high stress on components and heavy switching loss.These limitations drive towards innovative high-efficiency converter solutions for EV needs.

Table 1. Review of motors in EV application

Type of Motor	Key Features	Advantages	Limitations	Applications
DC Motor [3]	Brushed Design with simple control	Simple to operate and lower initial cost	High maintenance with lower efficiency and shorter lifespan.	Small electric devices and industrial applications
Induction Motor [4]	Rugged and has no commutators	Durable and reliable with cost-effectiveness.	Bulky Design with lower efficiency	Industrial drives and EVs like the Tesla Model S (initial models)
Synchronous Motor [5]	Rotates at synchronous speed with supply frequency	High efficiency and precise control	Complex and expensive and requires external excitation	Large industrial applications
Switched Reluctance Motor (SRM) [6]	Rotor has no windings and supports high-speed operation	Robust and reliable with low cost	High acoustic noise and complex control	Traction applications and pumps.
BLDC Motor [7]	Brushless Design with electronic commutation	Excellent speed-torque characteristics, low maintenance requirements, and high efficiency	Requires a complex motor controller and a higher initial cost	EVs, drones and robotics

In [11], a Boost-Cuk converter is presented providing continuous input and output currents, making it suitable for stable PV voltage boosting, but its bulky Design and high component count limit its practical use in compact EV systems. The Boost-SEPIC converter [12] ensures non-inverted output voltage and offers versatility in managing variable input voltages, but it suffers from increased component stress and switching losses. Similarly, super lift Luoconverter [13] achieves higher voltage conversion ratios with improved efficiency and reduced EMI, but its complexity poses challenges for implementation. As a result, the Boost-Zeta converter is introduced in this work, which addresses the drawback of other converters and provides a balanced trade-off between performance and reliability.

MPPT is made easier with this setup to guarantee the best possible use of solar energy. While other MPPT strategies maximise PV performance in EVs, the Perturb and Observe (P&O) method is straightforward and economical, but it has a reduced response time and oscillates around the MPP [14]. Although it provides quick and precise tracking, Incremental Conductance (IncCond) [15] is noise-sensitive. Hill Climbing [16] is fast and simple but can get stuck in local maxima and is noise-sensitive. The Artificial Neural Network (ANN) [17] method offers high adaptability and accuracy for PV systems but comes with computational complexity and requires extensive training data for effective implementation. These drawbacks emphasize the necessity of an optimization technique for effective PV use.

A popular technique because of its ease of use and quick convergence is Particle Swarm Optimization (PSO) [18], but it suffers from premature convergence. Grey Wolf Optimization (GWO) effectively balances exploration and exploitation but struggles with convergence speed in high-dimensional problems [19]. Ant Colony Optimization (ACO) [20] provides robust solutions by simulating pheromone-based search behavior, yet its computational complexity increases. Whale Optimization Algorithm (WOA) [21] excels in handling nonlinear problems but loses diversity in later iterations.

Similarly, Squirrel Search Algorithm (SSA) [21] and Coot Optimization Algorithm (COA) [22] have shown excellence for their dynamic exploration abilities; however, SSA suffer from slow convergence in complex scenarios. To overcome these limitations, this work proposes an improved Coot Optimization Algorithm (COA) to tune ANN parameters for MPPT. However, solar-powered EV systems face challenges such as inconsistency and nonlinear output characteristics, particularly under shaded conditions or during nighttime when solar energy availability is low.

Current converters have problems, including higher component stress and decreased efficiency. Conventional MPPT approaches also have drawbacks, such as poor reaction, inaccurate tracking, and noise sensitivity. Added to this, current systems lack integrated solutions for managing intermittent solar generation. Addressing these issues, this work includes advanced energy storage systems and a grid to maintain continuous operation and ensure reliability.

1.1. Research Contribution

Table 2 outlines the primary novel contributions of the proposed work, emphasizing the development of an eco-friendly PV-based EV charging system. The remainder of the research is structured as follows: The architecture and components of the proposed system are described in depth in Section II. The modeling of the system components is the main emphasis of Section III, the results and discussion are presented in Section IV, and the study is concluded with important conclusions in Section V.

Table 2. Contribution of research

Contribution	Description
Eco-Friendly EV Charging System	Utilizes a PV-based charging system to reduce grid dependency and minimize the carbon footprint of EV charging.
HGBZ Converter	To boost low PV voltage to suitable levels, ensuring efficient energy transfer when compared to existing ones.
ICO-ANN MPPT	To enhance power extraction under varying sunlight conditions for consistent charging with a faster response than classical algorithms.
Bidirectional DC-DC Converter	Allows energy storage of excess solar power and supplies power to EVs during low solar production, ensuring uninterrupted charging.
Grid Interaction via VSI	Incorporates 3ΦVSI for dynamic energy exchange with the grid, supporting grid stability.
Energy Management	Efficiently distributes excess solar energy to the grid or draws power when needed, optimizing energy utilization.

2. Proposed System Description

A RES integrating PV with BLDC motor EV application is presented in Figure 1, with grid and battery in addition, resulting in efficient energy management. The PV system acts as a primary source, with ICO-ANN MPPT, ensuring maximum extraction of power under changing conditions. The MPPT output is processed by a PWM generator that controls the operation of the proposed HGBZ converter, stepping the low PV voltage suitable for a BLDC motor of EV via a 3ΦVSI. A PWM generator manages the VSI signals, while the PI controller regulates the motor speed by comparing reference and actual speed, ensuring precise motor control.

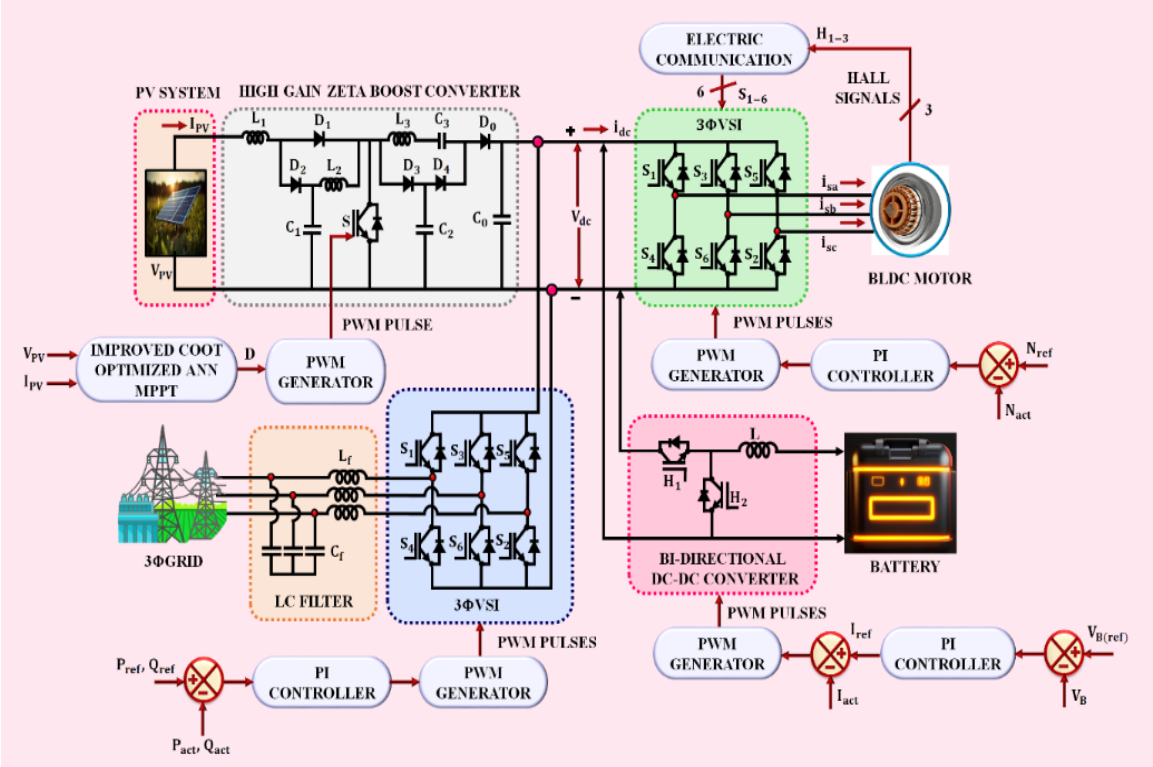

Fig. 1 HGBZ converter-equipped PV-based EV charging system proposal

Simultaneously, the battery system is connected via a bidirectional DC-DC converter supporting two-way energy transfer. The excess energy generated from PV and the grid supports charging the battery. While discharging it feeds power back to the DC bus to power the BLDC motor, at times of power demand from PV or the grid. PI controllers manage this by regulating both the current and voltage to maintain battery performance and safety.

The integration of the grid is accomplished by 3ΦVSI, converting DC voltage into an AC compatible with the grid. The low-pass filter minimizes harmonics, and PWM signals synchronize the inverter with the grid. Active and reactive power flow is controlled using a feedback loop matching reference value, ensuring energy balance. This demonstrates the system's effectiveness in efficient power control and improved energy harvesting.

3. Proposed System Modelling

3.1. PV With HGBZ Converter

PV system represents a significant advancement in renewable energy, providing solutions to align with growing energy demands. The system initiates with a solar cell, which, when connected in series, forms a PV module depicted in the equivalent circuit presented in Figure 2(a).

The PV module comprises a photocurrent sourceI_{Ph}, diode D and resistance in parallel and series R_{sh} andR_s. The relationship between output current and voltage for the equivalent circuit is given as:

$$I_{pv} = I_{ph} - I_{sh}\left(exp\left(\frac{V_{pv}+IR_s}{AN_sKT}\right) - 1\right) - \frac{V_{pv}+IR_s}{R_{sh}} \quad (1)$$

Saturation current is determined by I_{sh}, ideality factor of diode as A, charge of electron q, temperature T, Boltzmann constant k and series-connected cellsN_s Defines the operation of the PV system. The low voltage generated by PV needs boosting, which is accomplished in this work using the HGBZ converter shown in Figure 2(b). The switching waveform of the proposed HGBZ Converter, as shown in Figure 3, illustrates the dynamic operation of the converter's power switches during a complete switching cycle.

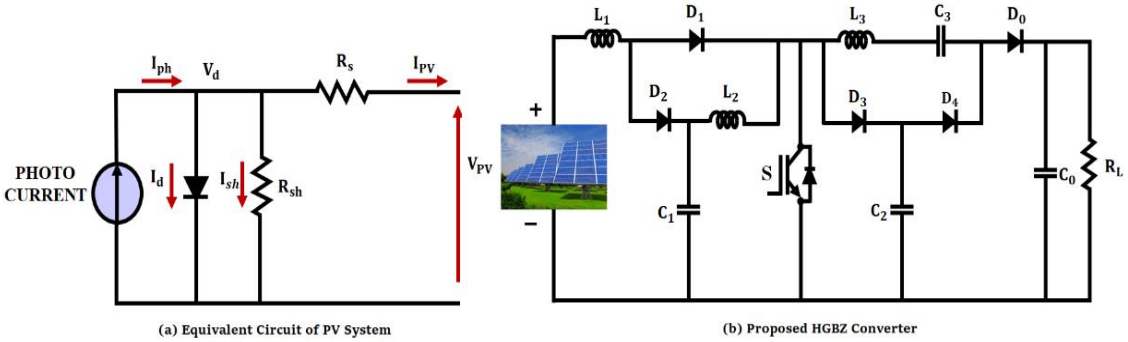

Fig. 2 Equivalent circuit configuration of (a) PV system, and (b) Proposed HGBZ converter.

3.1.1. Operating Modes of HGBZ Converter

Mode 1

In this mode, the switch shown in Figure 4(a) is in the conducting state, with the inductor L_1 is charged using a PV source V_{PV}. This causes current to flow through L_1, storing energy in its magnetic field. Inductor L_2 is connected in parallel with C_1, resulting in energy transfer from L_2 to C_1. This charges C_1 while regulating the current in L_2.

The capacitor C_2 andC_3 are charged through a diode D_4, which allows the output voltage to circulate to these capacitors. C_2 andC_3 They are designed to have equal voltage levels on average owing to the symmetrical configuration of the circuit. This ensures balanced energy distribution between these capacitors. The output capacitor C_0ensures a smooth output voltage by mitigating ripples. This stored energy is delivered to the load R_L, maintaining stable operation.

$$V_{L_1} = V_{PV} \quad (2)$$

$$V_{L_2} = V_{PV} \quad (3)$$

Mode 2

During this mode, the switch is turned OFF, as seen in Figure 4(b), and the previously stored energy in the inductors L_1 to L_2 is released. This energy transfer occurs through diodes D_2, D_3, D_4 and D_0 to the corresponding capacitors and load R_L. Inductor L_1, charged during the ON phase of the switch, releases its energy through the diode D_2 to capacitor C_1, ensuring C_1 maintains its charge level. The energy stored in C_1 is transferred via L_3 and diode D_3 to C_2 andC_3, and eventually through the diode D_0 to the output capacitor C_0 and load R_L. Capacitor C_2 andC_3 are charged through energy flow facilitated by diodes D_3 and D_4. Thereby, the voltages remain balanced due to the symmetrical nature of the circuit.

$$V_{L_1} = V_{PV} - V_{C_1} \quad (4)$$

$$V_{L_2} = V_{C_1} - V_{C_3} \quad (5)$$

On applying the second balance law to the inductor L_1 and L_2

$$\int_0^{DT_s} V_{PV}\, dt + \int_{DT_s}^{T_s} (V_{PV} - V_{C_1})\, dt = 0 \quad (6)$$

$$\int_0^{DT_s} V_{C_1}\, dt + \int_{DT_s}^{T_s} (V_{C_1} - V_{C_3})\, dt = 0 \quad (7)$$

On solving Equation (6)

$$V_{C_1} = \frac{V_{PV}}{(1-D)} \quad (8)$$

By substituting Equation (8) into Equation (7), the values of V_{C_2} and V_0 is determined as

$$V_{C_3} = \frac{V_{PV}}{(1-D)^2} \quad (9)$$

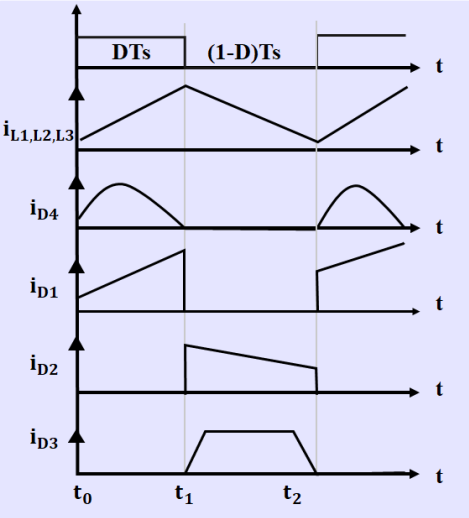

Fig. 3 Switching operation of HGBZ converter

Voltage gain at CCM is expressed as

$$\frac{V_0}{V_{PV}} = \frac{1}{(1-D)^2} \tag{10}$$

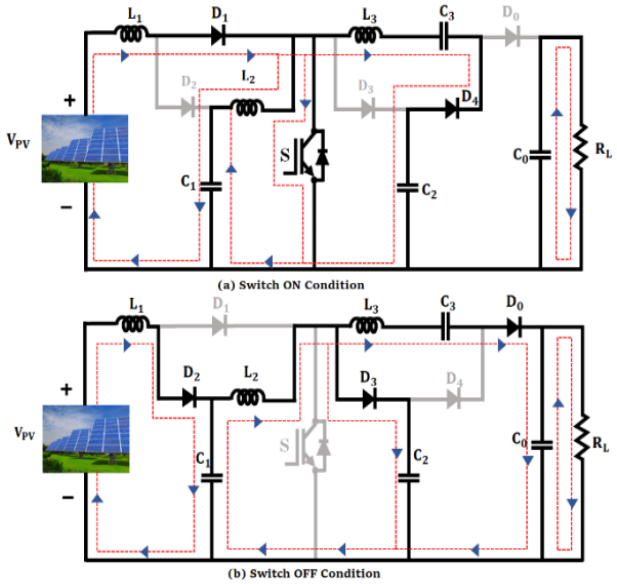

Fig. 4 Operation of proposed HGBZ converter (a) Switch ON, and (b) Switch OFF.

3.1.2. Design of inductors

During the switch-on scenario, the peak ripple relation of the inductor L_1 and L_2 is attained as follows

$$\Delta i_{L_1} = \frac{V_{PV} DT}{L_1} \tag{11}$$

On solving L_1,

$$L_1 > \frac{(1-D)^4 D R_L}{2 f_s} \tag{12}$$

Similarly for L_2

$$\Delta i_{L_2} = \frac{V_{C_1} DT}{L_2} \tag{13}$$

On substituting $V_{C_1} = \frac{V_{PV}}{(1-D)}$, the design expression becomes

$$L_2 > \frac{(1-D)^2 D R_L}{2 f_s} \tag{14}$$

3.1.3. Design of Capacitors

Capacitor design depends on ripple voltage and current. General design equations for input and output capacitors are as follows:

The input capacitor helps maintain a stable voltage at the input side by filtering voltage ripples caused by the switching action.

$$C_1 = \frac{I_0 D}{(1-D) f_s \Delta V_{C_1}} \tag{15}$$

Where the load current is noted as I_0, and ΔV_{C_1} represents the allowable ripple voltage across C_1. The output capacitor smooths the output voltage and ensures stable delivery to the load.

$$C_0 = \frac{I_0 D}{f_s \Delta V_{C_0}} \tag{16}$$

ΔV_{C_0} defines the allowable ripple voltage across C_0.

3.1.4. Analysis of Power Loss

Power loss in the HGBZ converter occurs due to various components, directly impacting efficiency.

Switching Loss: The switch experiences conduction losses when it is ON due to its internal resistance $R_{DS(on)}$.

$$P_S = I^2_{S(rms)} R_{DS(on)} \tag{17}$$

Where the RMS current through the switch is noted as $I_{S(rms)}$.

Diode Loss: Diodes contribute to two types of losses:

Conduction Loss (P_{R_F}): Caused by resistance R_F of a diode.

$$P_{R_F} = \sum I^2_{D(rms)} R_F \tag{18}$$

Forward Voltage Drop Loss (P_{V_F}): Due to the forward voltage dropV_F of a diode.

$$P_{V_F} = \sum I_{D(avg)} V_F \tag{19}$$

Inductor Loss: Inductor losses occur due to the winding resistance R_L of an inductor.

$$P_L = I_{L_1(rms)}^2 R_{L_1} + I_{L_2(rms)}^2 R_{L_2} + I_{L_3(rms)}^2 R_{L_3} \quad (20)$$

Minimized by selecting inductors with low resistance and high-quality cores.

Capacitor Loss: Caused by Equivalent Series Resistance (ESR) of capacitors.

$$P_C = \sum I_{C(rms)}^2 R_{ESR} \quad (21)$$

The proposed HGBZ converter offers a compact solution to power an EV motor with high gain in voltage, ripple-free current and reduced stress on components to enhance system performance. The regulation of the converter depends on the controller, which is discussed as follows.

3.2. Improved Coot Optimized ANN MPPT Controller

An ANN-based MPPT controller is a sophisticated technique for optimizing the power output of a PV system. The ANN uses its ability to model complex, nonlinear relationships, enabling precise tracking of MPP under changing conditions, including temperature and irradiance. The ANN architecture comprises three layers, where the input layer receives parameters such as solar irradiance, temperature and PV arrays voltage and current. These inputs are processed by a hidden layer, using weights, biases, and nonlinear activation functions to learn the intricate pattern. Followed by an output layer generating a control signal, typically a duty cycle, that is applied to the converter, which adjusts the PV arrays' voltage and current to align with MPP.

The weights and biases are optimally tuned in this work to improve ANN performance further using the ICO Algorithm. A flow chart illustration of the proposed ICO-ANN MPPT is presented in Figure 5. The optimization approach mimics the behavior of coot birds in search space, where each particle represents a set of potential ANN parameters. The weights $W_{i,j}$ and biases b_i of ANN are represented as particles X_i In the ICOA search space. The expression is given by

$$X_i = [W_{i,j}, b_i] \quad (22)$$

Each particle corresponds to a potential solution for the ANN parameter set. The goal is to ensure that the ANN predicts the duty cycle accurately, leading to maximize power extraction. Instead of random initialization, fixed initial positions are utilized to enhance the convergence. Each initial position corresponds to a specific duty cycle, ensuring a well-distributed search space and avoiding overlapping in regions near MPP. Each coot position $D_i(k)$ is calculated depending on the power output $P_i(k)$, predicted by the ANN at that position. The objective function is typically the Mean Squared Error (MSE) for ANN training:

$$MSE = \frac{1}{N}\sum_{k=1}^{N}\left(P_{pred}(k) - P_{actual}(k)\right)^2 \quad (23)$$

Where the predicted power by ANN is noted as $P_{pred}(k)$ and actual power output from PV as $P_{actual}(k)$. The goal is to minimize MSE, which guarantees the ANN predicts accurate duty cycles. After the power output $P_i(k)$ at each coot's position is compared with its personal best power $P_{besti}(k)$:

$$\begin{cases} P_{besti}(k) > P_{besti}(k-1) \\ P_{besti}(k) = P_i(k) \\ D_{besti}(k) = D_i(k) \end{cases} \quad (24)$$

Once all coots have been evaluated, the global best $P_{Gbest}(k)$ is determined,

$$P_{Gbest}(k) = max(P_{best,1}(k), P_{best,2}(k), \dots) \quad (25)$$

The corresponding duty cycle position is indicated as $D_{Gbest}(k)$, ensuring that the algorithm identifies both the best individual solutions for optimizing ANN parameters. The search process ends when $P_{Gbest}(k)$ And that is D_i meets the convergence criteria

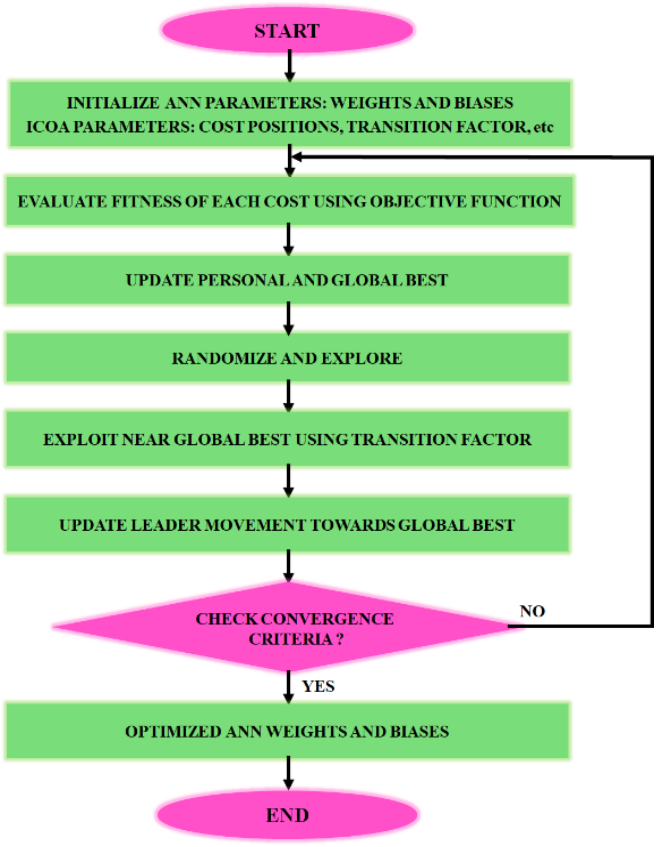

Fig. 5 Flow chart illustration of ICO-ANN MPPT

$$\frac{|P_{Gbest}(k)-P_{Gbest}(k-1)|}{P_{Gbest}(k-1)} < 0.05 \quad (26)$$

This states that the change in global best power across iterations is less than 5%. The proximity of the coot position is $\Delta D < 0.05$, representing the position of coots that converge to a common solution. These conditions guarantee that the algorithm has accurately located the Global Maximum Power Point (GMPP). In ICOA, the randomization phase is adjusted to address the issues in tuning the weights and biases of the ANN. Notably, the random factor R is modified from the range [-1,1] to [0,1]. This change ensures the updated ANN parameters remain within the defined limits, avoiding invalid updates. The exploration (global search) and exploitation (local refinement) phases are crucial for finding the global optimum in ICOA, particularly during ANN parameter tuning. To address this, the Transition Factor (TF) is introduced, dynamically balancing exploration and exploitation during the optimization process, given by

$$TF = Ce^{(L/Iter)} \quad (27)$$

Where C represents a constant parameter with default value 2, L indicates current iteration, and $Iter$ specifies the total number of iterations. The ICOA updates the position of coots when the convergence condition in Equation (26) and $\Delta D < 0.05$ is not satisfied. To further optimize MSE, the updated position of the coot is expressed as

$$D_i(k+1) = 1 \times R_1 \times cos(2\pi R) \times (D_{Gbest}(k) - D_i(k)) + D_{Gbest}(k) \quad (28)$$

Where the coot position is determined as $D_i(k)$, Random numbers in the range [0,1] are indicated as $R_1$and the global best position is noted as $D_{Gbest}(k)$. The random motion phase improves the search space exploration by modifying the particles to update their positions relative to the global best. Replace random positions (W) with the best global position:

$$W = D_{Gbest}(k) \quad (29)$$

Update the position of the coot

$$D_i(k+1) = D_i(k) + S.TF.abs(D_{Gbest}(k) - D_i(k)) \quad (30)$$

The shrinking factor

$$S = 2 - L\left(\frac{1}{Iter}\right) \quad (31)$$

The shrinking factor and transition factor ensure that the search becomes more focused as iterations progress. This helps in refining ANN parameters after an initial broad search. By replacing the random position W with the global best $D_{Gbest}(k)$, the ANN parameters $W_{i,j}$ and b_iThey are tuned closer to their optimal values, reducing prediction error. Chain motion is modified to average the current and previous positions of coots:

$$D_i(k+1) = 0.5.(D_i(k+1) + D_i(k) \quad (32)$$

This smoothens parameter updates, reducing fluctuations in training and improving ANN convergence. Next, the ICOA introduces changes to leader movement to ensure convergence towards a global optimum solution with controlled randomization. This mechanism significantly enhances the accuracy and convergence speed when tuning weights and biases of an ANN for MPPT. The leader's position,$D_{Gbest}(k)$ is updated based on a probability-based rule $(P = 0.5)$, ensuring the group progresses toward g_{best} while introducing controlled randomness

$$D_{Gbest}(k) = \begin{cases} C.cos(2\pi R) \times TF \times abs(g_{best} - (D_{Gbest}(k)) + g_{best}R < 0.5 \\ C.cos(2\pi R) \times TF \times abs(g_{best} - (D_{Gbest}(k)) - g_{best}R > 0.5 \end{cases} \quad (33)$$

Where g_{best} Determines the best position attained and $C = 2 - L\left(\frac{1}{Iter}\right)$. Once the MPPT and termination conditions are satisfied, the algorithm monitors the PV system for changes in input power. (P_{PV}) or maximum power point (P_{MPP}):

$$\frac{|P_{MPP}-P_{PV}(k)|}{P_{MPP}} > 0.05 \quad (34)$$

The reset mechanism allows ANN parameters to adapt to real-time changes in environmental conditions, maintaining high prediction accuracy for MPPT. Thus, precise tracking of MPP is attained with the integration of ANN with ICOA. Weights and biases of the ANN are tuned by ICOA for minimizing MSE. By altering the random range to [0, 1], the process of searching is improved. Added to this, group convergence is ensured by updating the probabilistic leader, thereby maintaining solution diversity. Thus, the incorporation of ICOA with ANN improved the robustness of maximum power tracking.

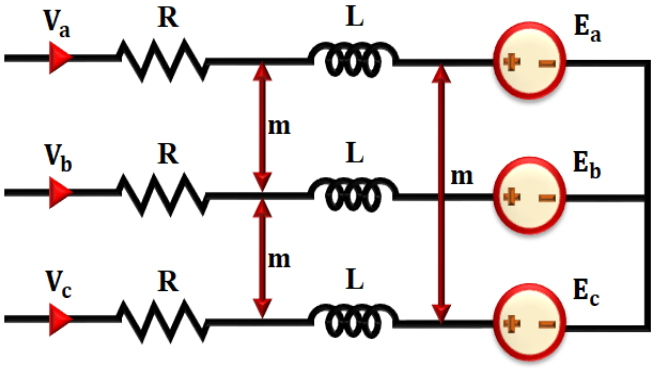

Fig. 6 BLDC motor analogous circuit

3.3. BLDC Motor Modelling with PI Controller for Speed Control

In this work, the EV uses a BLDC motor, and in Figure 6, the analogues circuit is represented. In the configuration, the rotor of the BLDC motor is composed of permanent magnets, generating the magnetic field. In addition, the motor includes symmetrical windings that generate trapezoidal back Electro Motive Force (EMF). The rotor current is considered negligible due to the higher resistances of permanent magnets.

The operation of the BLDC motor is driven by the interaction between the magnets and windings. The stator voltage is computed as

$$V_a = r.I_a + L\frac{dI_A}{dt} + \left[\frac{dI_b}{dt} + \frac{dI_c}{dt}\right] + E_a \quad (35)$$

$$V_b = r.I_b + L\frac{dI_B}{dt} + \left[\frac{dI_a}{dt} + \frac{dI_c}{dt}\right] + E_b \quad (36)$$

$$V_c = r.I_c + L\frac{dI_C}{dt} + \left[\frac{dI_b}{dt} + \frac{dI_a}{dt}\right] + E_c \quad (37)$$

In a balanced system

$$I_a + I_b + I_c = 0 \quad (38)$$

The matrix form for voltage is expressed as

$$\begin{bmatrix} V_a \\ V_b \\ V_c \end{bmatrix} = \begin{bmatrix} r & 0 & 0 \\ 0 & r & 0 \\ 0 & 0 & r \end{bmatrix}\begin{bmatrix} I_a \\ I_b \\ I_c \end{bmatrix} + \frac{d}{dt}\begin{bmatrix} L-M & 0 & 0 \\ 0 & L-M & 0 \\ 0 & 0 & L-M \end{bmatrix}\begin{bmatrix} I_a \\ I_b \\ I_c \end{bmatrix} + \begin{bmatrix} E_a \\ E_b \\ E_c \end{bmatrix} \quad (39)$$

The expression for phase-to-phase voltage is calculated as,

$$V_{ab} = r(I_a - I_b) + (L-M)\frac{d}{dt}(I_a - I_b) + E_{ab} \quad (40)$$

$$V_{bc} = r(I_b - I_c) + (L-M)\frac{d}{dt}(I_b - I_c) + E_{bc} \quad (41)$$

As the system is balanced, mutual inductance is neglected,

$$\frac{dI_a}{dt} = \frac{r}{L}I_a + \frac{2}{3L}(V_{ab} - E_{ab}) + \frac{2}{3L}(V_{bc} - E_{bc}) \quad (42)$$

$$\frac{dI_b}{dt} = \frac{r}{L}I_b + \frac{2}{3L}(V_{ab} - E_{ab}) + \frac{2}{3L}(V_{bc} - E_{bc}) \quad (43)$$

The Back EMF phase is given by

$$E_a = K\omega F(\theta) \quad (44)$$

$$E_b = K\omega F(\theta - \frac{2\Pi}{3} \quad (45)$$

$$E_c = K\omega F(\theta + \frac{2\Pi}{3} \quad (46)$$

Where the motor constant is defined by K, the position function is noted as $F(\theta)$ and the angular speed is specified as ω. The BLDC motor torque is expressed by

$$T = \frac{E_aI_a + E_bI_b + E_cI_c}{\omega} \quad (47)$$

The three-phase back EMF is given by

$$T_a = K_tI_aF(\theta) \quad (48)$$

$$T_b = K_tI_bF(\theta - \frac{2\Pi}{3} \quad (49)$$

$$T_c = K_tI_cF(\theta + \frac{2\Pi}{3} \quad (50)$$

$$T_{em} = T_a + T_b + T_c \quad (51)$$

The mechanical expression of the motor is given

$$J\frac{d\Omega}{dt} = T_{em} - T_L - F_\Omega \quad (52)$$

Where $\theta_e = \frac{p}{2}\theta$ and $\omega = \frac{d\theta}{dt}$

Speed control is crucial for ensuring a BLDC motor operates at the desired speed. The PI controller is an effective method widely adopted owing to its simplicity. This ensures that the motor operates at the desired speed by minimizing the error between reference and actual speed. Integral and proportional components are combined by a PI controller, shown in Figure 7, to generate an output signal. The PI controller equation is represented by

$$y(t) = K_pe(t) + \frac{K_p}{T_i}\int_0^1 e(t)dt \quad (53)$$

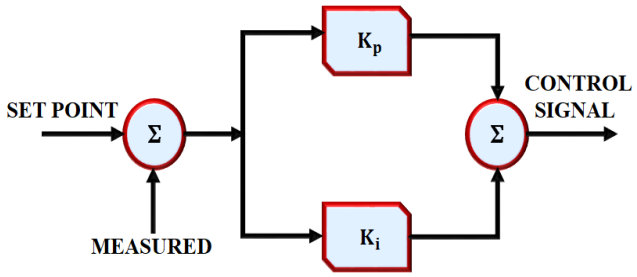

Fig. 7 Schematic representation of PI controller

The input signal regulated is represented by $e(t)$, while the output signal is noted as $y(t)$. The three adjustable parameters include the time constant and proportionality gain. K_p and integral time constant T_i. These parameters are typically expressed as coefficients to construct the transfer function.

$$G(s) = K_p + \frac{K_i}{s} \quad (54)$$

The combined output of the PI controller generates PWM pulses to the VSI, regulating voltage and current supplied to the BLDC motor. This ensures smooth and stable speed control, effectively reducing steady-state error while ensuring efficient performance under varying loads.

3.4. Grid Synchronization

A Phase-Locked Loop (PLL) is a robust synchronization method that accurately detects the phase angle of grid voltages, even in noisy or harmonic-rich conditions, as shown in Figure 8. It operates in the dq reference frame, where the three-phase voltage e_{abc}It is converted into steady DC components via Park transformation.

$$\begin{bmatrix} e_d \\ e_q \end{bmatrix} = \begin{bmatrix} cos(\theta) & cos(\theta - \frac{2\pi}{3}) & cos(\theta + \frac{2\pi}{3}) \\ -sin(\theta) & -sin\left(\theta - \frac{2\pi}{3}\right) & -sin\left(\theta + \frac{2\pi}{3}\right) \end{bmatrix} \begin{bmatrix} e_a \\ e_b \\ e_c \end{bmatrix} \quad (55)$$

To enable phase detection, the PLL sets the desired direct-axis voltage component. e_d^*To zero.

$$error = e_d^* - e_d \quad (56)$$

A PI controller eliminates phase error, functioning as a loop filter.

$$u(t) = K_p e_{error} + K_i \int e_{error} dt \quad (57)$$

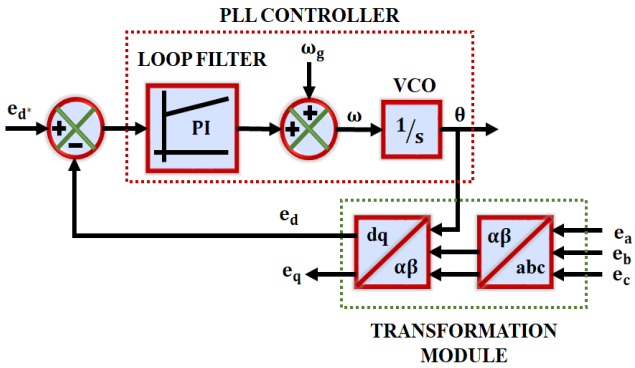

Fig. 8 Structure of PLL for grid synchronization

The resulting signal, along with the nominal grid frequency ω_{ff}defines the grid frequency as

$$\omega = \omega_{ff} + ut(t) \quad (58)$$

The output is fed into a Voltage-Controlled Oscillator (VCO), often implemented as an integrator, to generate the synchronized phase angle (θ).

$$\theta = \int \omega dt \quad (59)$$

The equations enable precise alignment of the inverter's output with the grid's voltage phase, frequency and amplitude.

3.5. Battery Energy Storage System

In order to transform chemical energy into electrical energy, a rechargeable electrochemical battery is also used, which consists of several battery cells grouped into modules and several modules into a battery system. BESS collects and stores energy from the electrical grid or renewable energy sources.

Batteries then discharge and release energy during periods of high demand, power interruptions, and even low RES energy productivity. Figure 9 shows the bidirectional power supply required for battery charging and discharging.

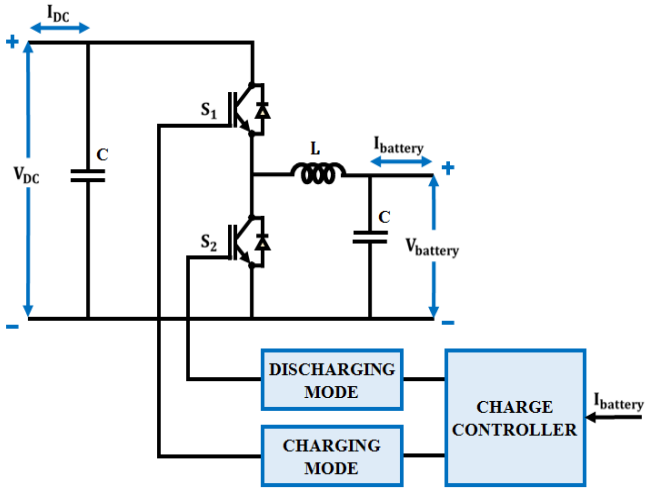

Fig. 9 Bidirectional converter for battery

In relation to its volume, the battery's State of Charge (SOC) is determined by

$$SOC = 100\left(1 + \frac{\int I_{ESS} dt}{Q}\right) \quad (60)$$

In this case, I_{ESS} Battery charging current and Q-battery capacity.

Buck mode facilitates battery charging by using the DC-link as the source and the ESS as the load. On the other hand, ESS is the source in boost mode when the converter permits the battery to discharge.

4. Results and Discussion

This section evaluates the proposed PV-based EV charging system to demonstrate its efficiency, sustainability, and reliability. Table 3 offers the detailed specifications of the system components. The simulation is done using MATLAB, validating the effectiveness of the system.

Table 3. Design Parameters

Parameter	Description	Parameter	Description
Solar PV System			
Peak Power	10kW	Capacity	500W
Short circuit Current	8.95A	Maximum power Voltage	29.95V
Maximum Current	8.35A	Open circuit Voltage	37.25V
High-gain Zeta-Cuk converter			
Switching Frequency	10kHz	L_1, L_2, L_3	4.7mH
C	22μF	C_o	2200 μF

4.1. Scenario 1: Steady State Condition

The effectiveness of the proposed HGBZ converter under steady state conditions is represented in Figure 9. Depending on the case 1 scenario, the temperature and irradiance are noticed to be constant, maintained at 35℃ and $1000W/m^2$. According to this scenario, the input voltage to the converter attained from the PV system is 200V with a current measuring of about 45A, oscillating at the initial phase. In relation to the input from the PV system, the proposed converter shows boosted performance, as seen in Figure 11.

The HGBZ converter ranks with an improved voltage of 600V, with slight oscillations at the start-up period. Whereas, the current waveform of the converter reveals an initial peak rise in voltage after gradually reducing and continues at 14.3A, without any further fluctuations.

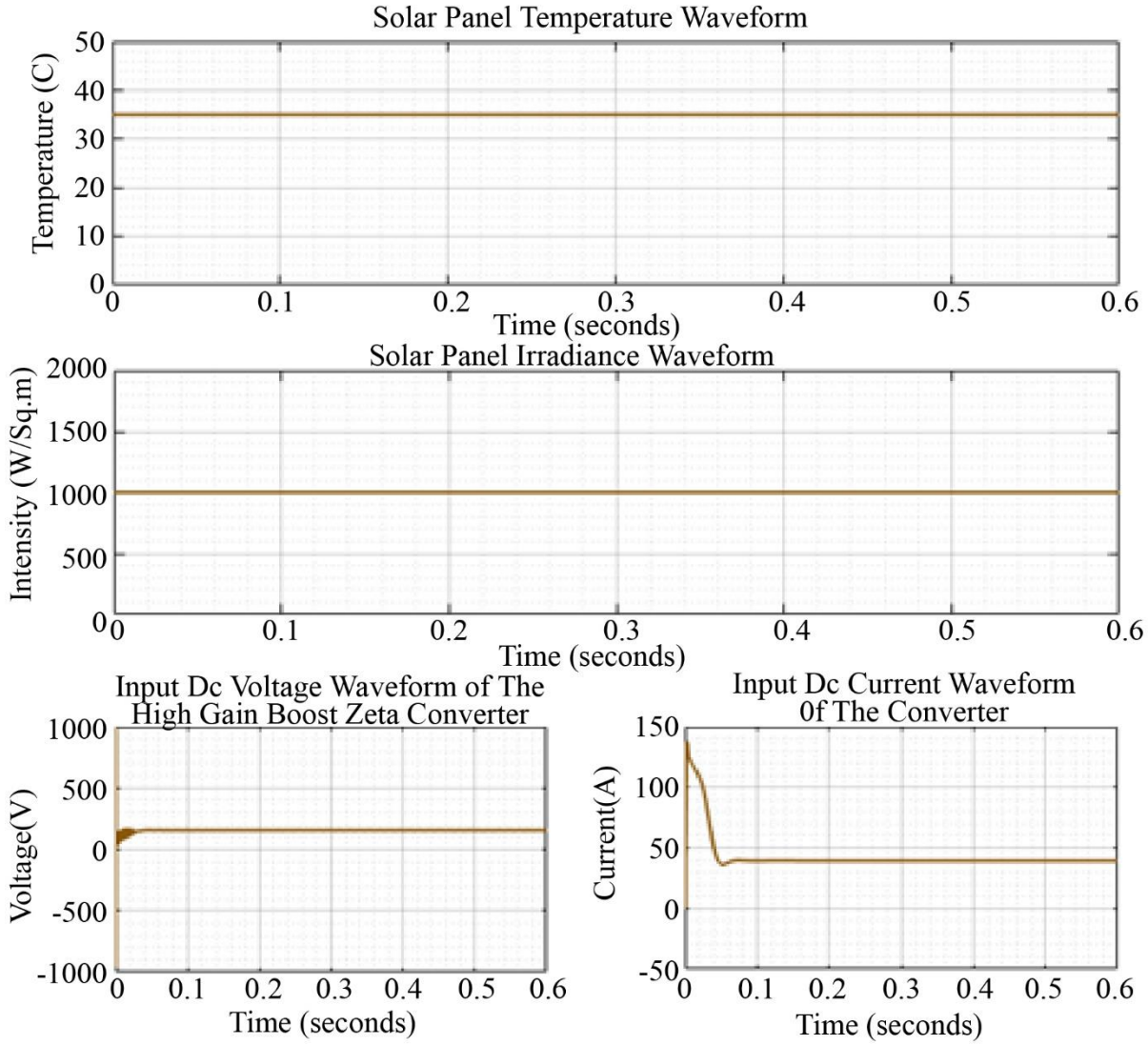

Fig. 10 PV under steady state condition

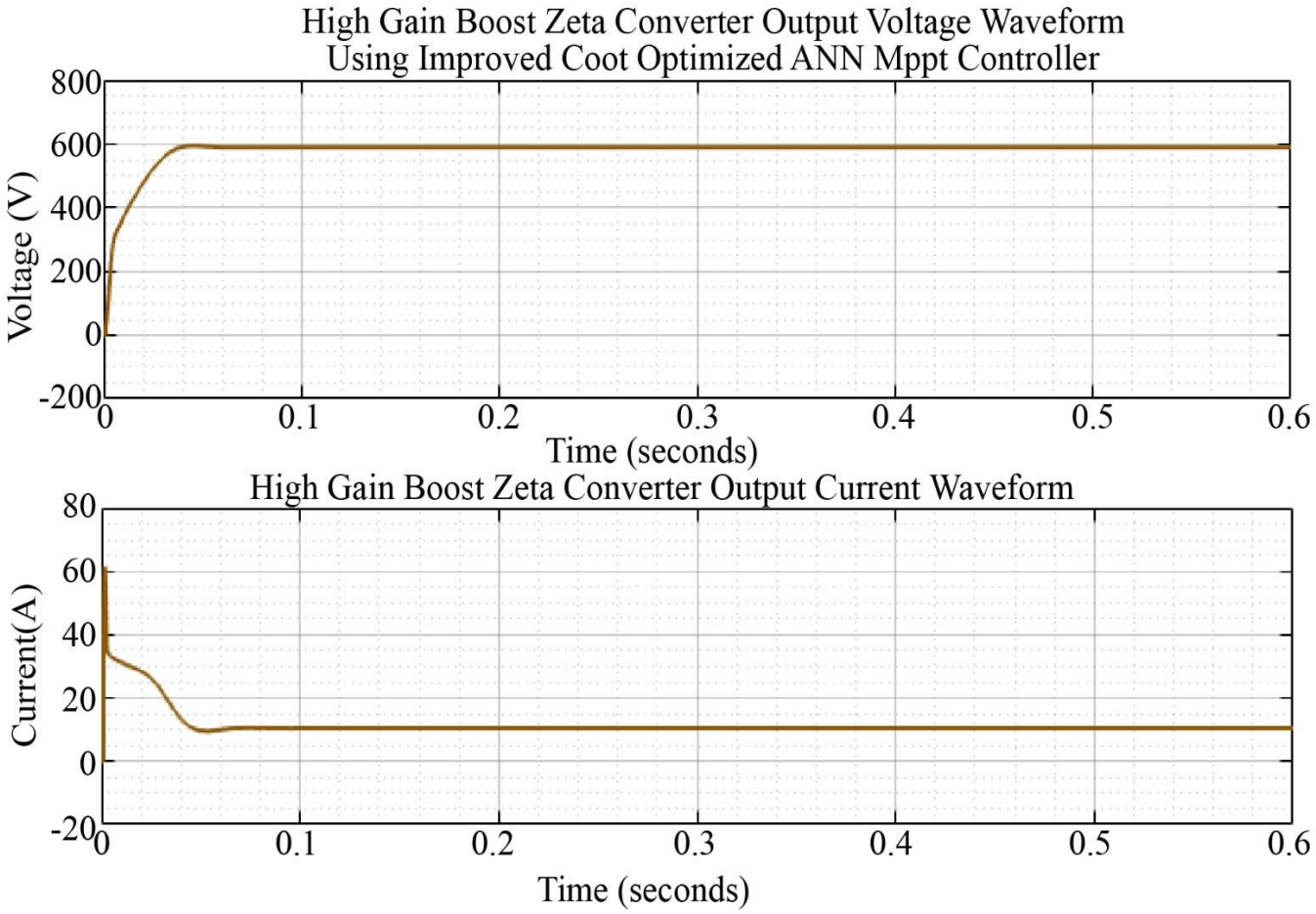

Fig. 11 Proposed converter output

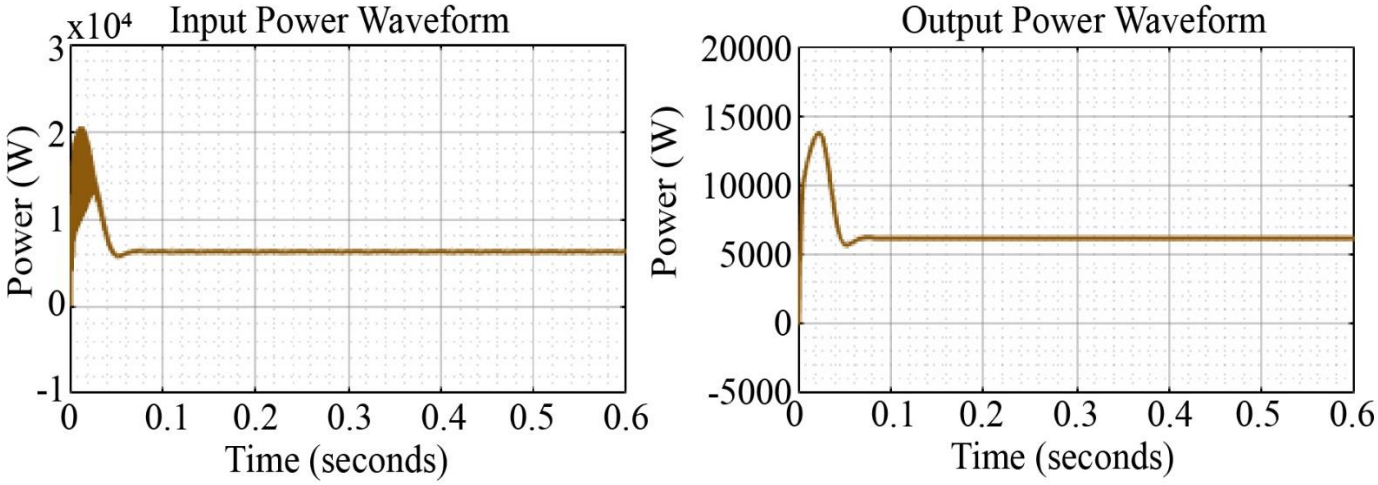

Fig. 12 Input/output characteristics

The power waveform of the proposed converter under steady state conditions is illustrated in Figure 12. With peak rise power at the initial period, the system accomplishes a steady current of 9000W.

Meanwhile, the proposed converter, together with the assistance of ICO-ANN MPPT, results in a rise in oscillations, resulting in a steady output power of 8700W being attained, with no more oscillations.

4.2. Case 2: Varying Temperature and Irradiance

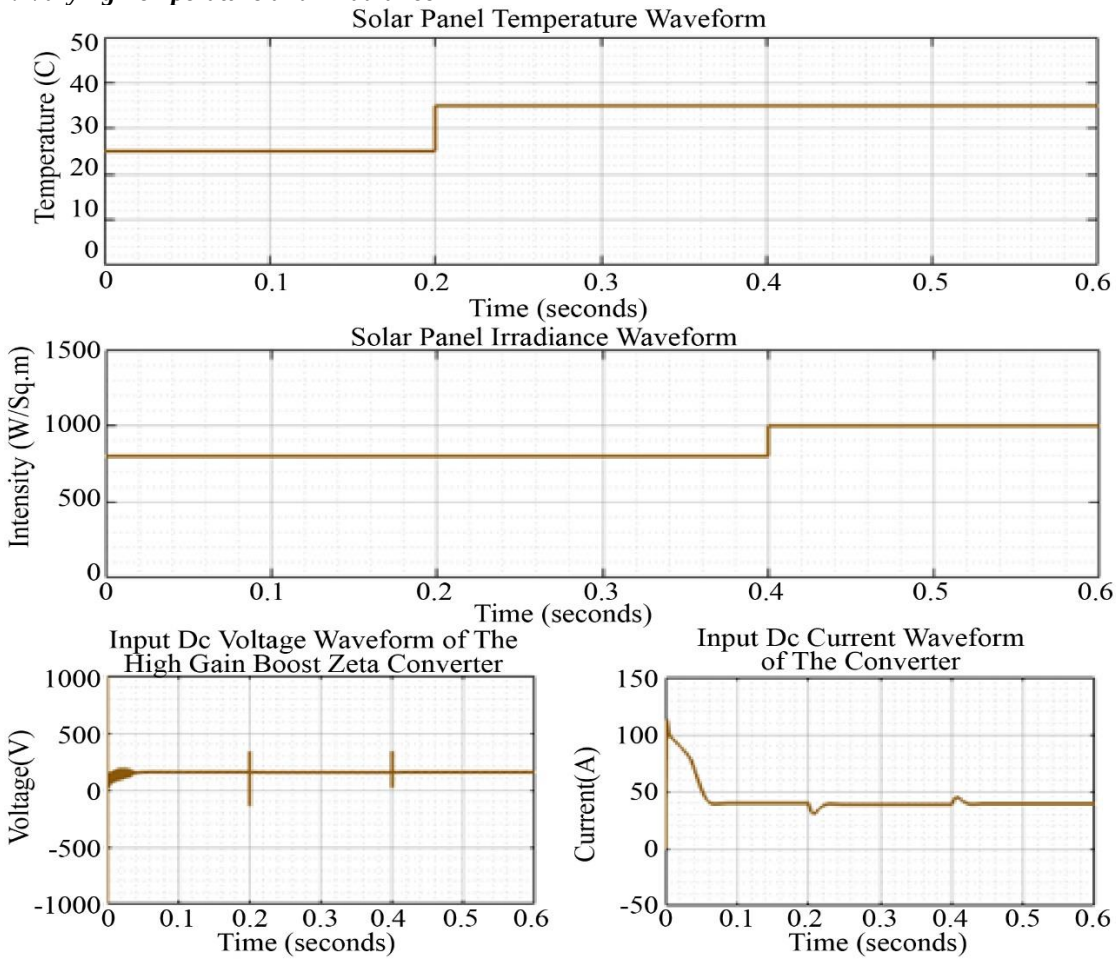

Fig. 13 PV under case 2 scenario

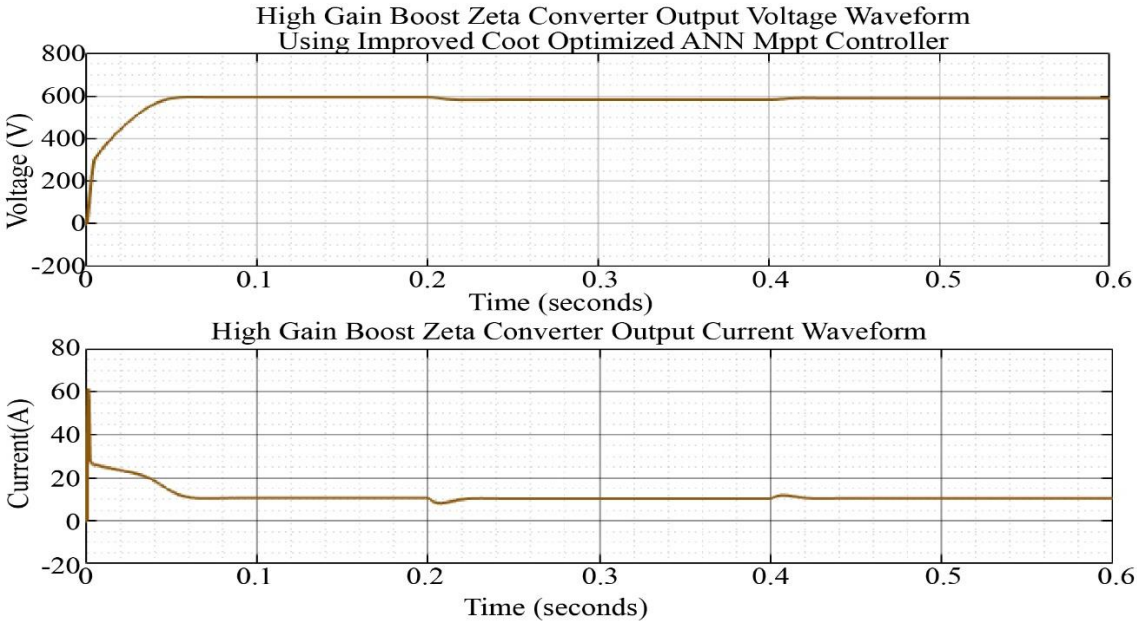

Fig. 14 Output characteristics of hgbz converter

The performance of the proposed converter under case 2 Scenario is demonstrated in Figure 13. The temperature waveform is noticed to be maintained at 30℃, and after 0.2s, the temperature increases and continues at 35℃. In contrast, the irradiance waveform is noticed to be maintained at $800W/m^2$, after 0.4s, the level of irradiance gets increased and sustains at $1000W/m^2$. The enhanced performance of the proposed HGBZ converter is represented in Figure 14. Converter output voltage rises initially and continues at 600V with slight oscillations.

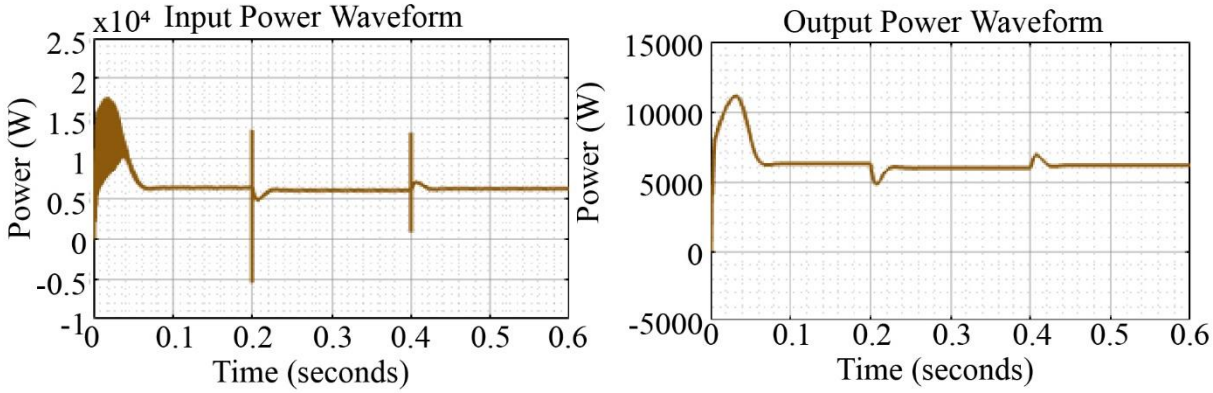

Fig. 15 Power characteristics under case 2

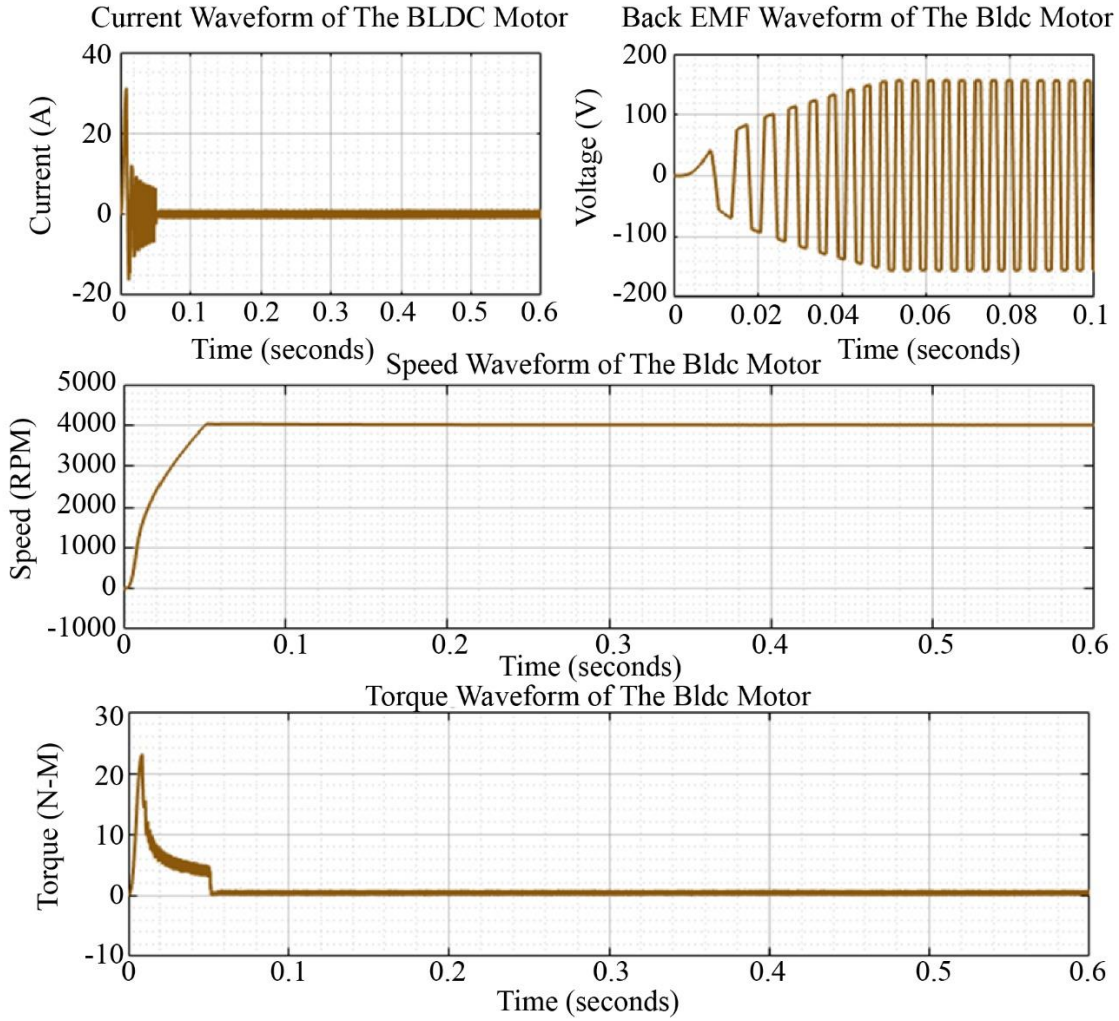

Fig. 16 Performance waveforms of BLDC motor

After 0.4s, the voltage gets stabilized and continues further without distortions. Likewise, the current gradually increases and reaches a peak value, after decreasing and continues at 14.3A with oscillation owing to the changing condition of PV temperature and irradiance, and settles after 0.4s. Figure 15 shows the input power waveform of the PV array and the output power waveform after conversion by the HGBZ converter. The input power stabilizes at around 9000W after initial transients, demonstrating effective MPPT performance. The output power waveform reaches approximately 8700W, indicating efficient energy conversion and consistent delivery for EV charging. Figure 16 depicts the performance characteristics of the BLDC motor during operation. The current waveform shows stabilization after an initial surge, while the back EMF waveform reflects sinusoidal behavior, indicating smooth motor operation. The speed waveform demonstrates rapid acceleration to 4000 RPM, achieving steady-state within 0.1 seconds. The torque waveform indicates an initial peak followed by stabilization, highlighting efficient motor performance.

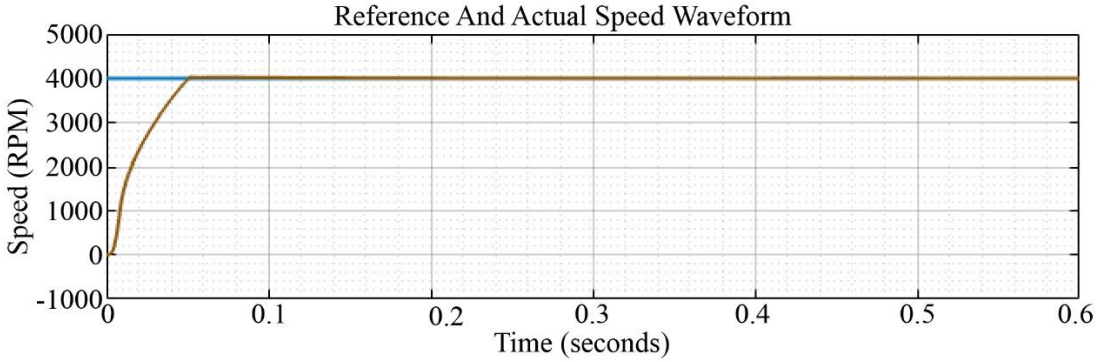

Fig. 17 Reference and actual speed waveform of BLDC motor

The BLDC motor speed comparison waveform is illustrated in Figure 17, between the actual and reference speed. The waveform demonstrates that the actual speed rapidly converges to the reference speed of 4000 RPM within 0.1 seconds, demonstrating precise speed tracking and effective control.

4.3. BLDC Motor Performance with a load of 1NM at 0.3s

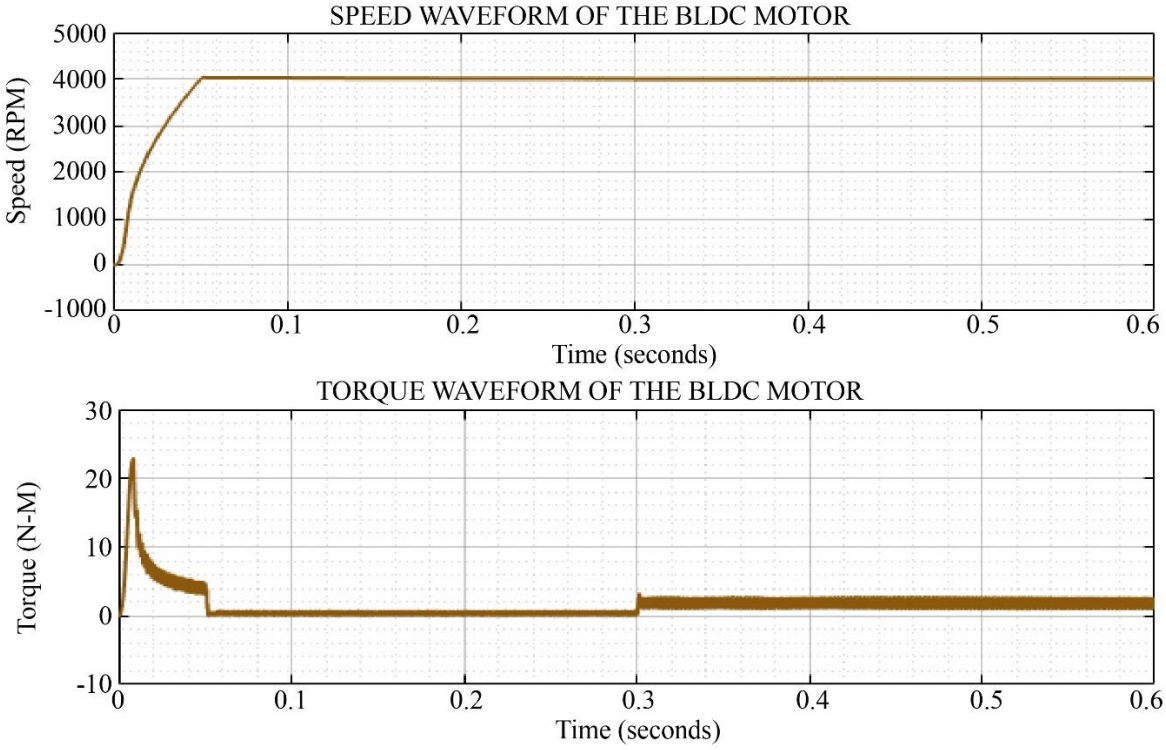

Fig. 18 Speed and torque waveform of BLDC motor with 1NM load

Assessment of the BLDC motor by applying a load of 1N · m at 0.3s is illustrated in Figure 18. It is seen that, on applying load, the speed of the BLDC motor remains unchanged and continues at 4000RPM, indicating the motor's ability to maintain consistent performance despite load conditions. Whereas the torque waveform reflects transient response at the starting period and stabilize after 0.3s, revealing the efficiency of the motor in handling the load.

4.4. BLDC Motor Performance with a Load of 1.5NM at 0.3s

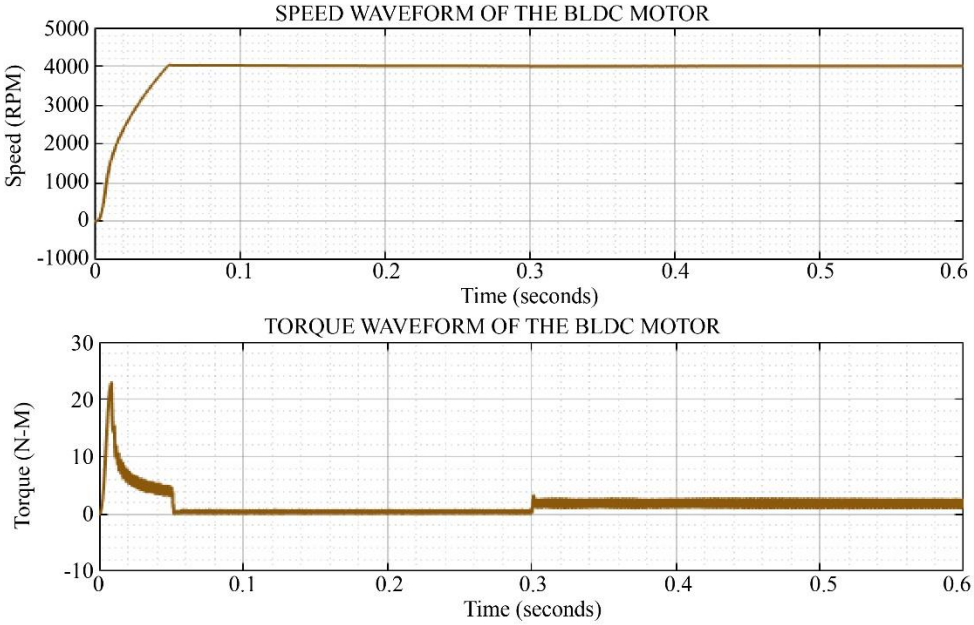

Fig. 19 BLDC Motor speed and torque waveform Under 1.5NM load condition

The performance of the BLDC motor under 1.5NM load is demonstrated in Figure 19. The speed waveform shows a rapid increase to 4000RPM, accomplishing steady state within 0.1s, even after applying a load of 1.5NM. In correspondence, the torque waveform determines initial oscillations and remains constant after 0.3s, respectively.

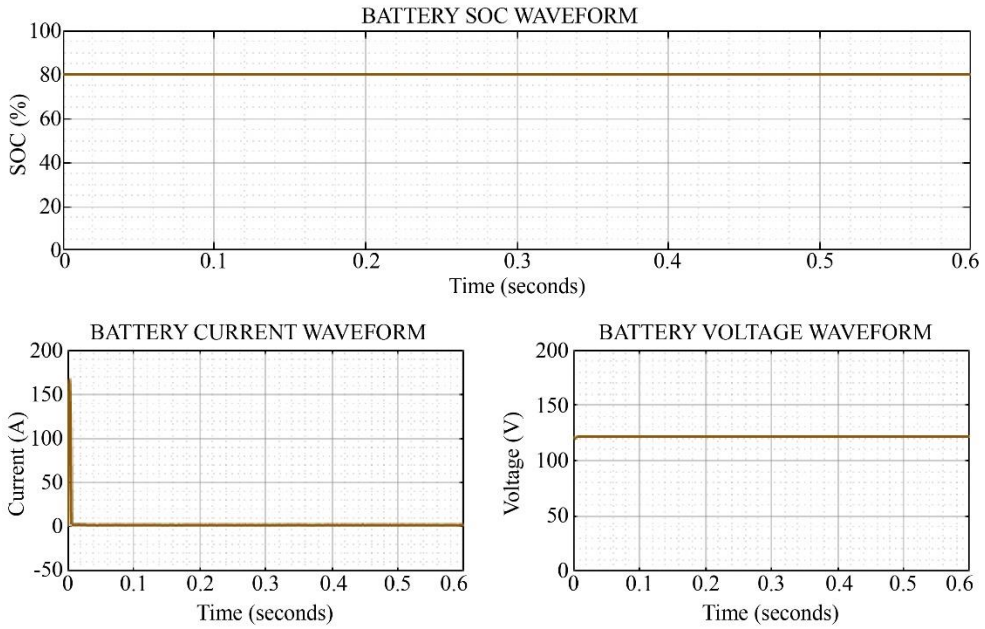

Fig. 20 Battery characteristics waveform

The illustration of battery performance in PV-based EV charging systems is shown in Figure 20. The SOC waveform indicates a steady value of 80%, demonstrating balanced usage of energy without overcharging throughout the period. The current waveform of the battery remains stable at a minimal value, ensuring consistent flow to support charging. Simultaneously, the voltage waveform demonstrates a constant value of 120V, indicating the system's ability to maintain stable voltage levels.

The waveform representing grid voltage, current, and in-phase performance is represented in Figure 21. The grid voltage waveform demonstrates stabilized voltage measuring 415V, with a current of 12A, demonstrating stable grid interaction.

The grid's combined voltage and current waveform highlights synchronization, revealing efficient transfer and reduced distortion.

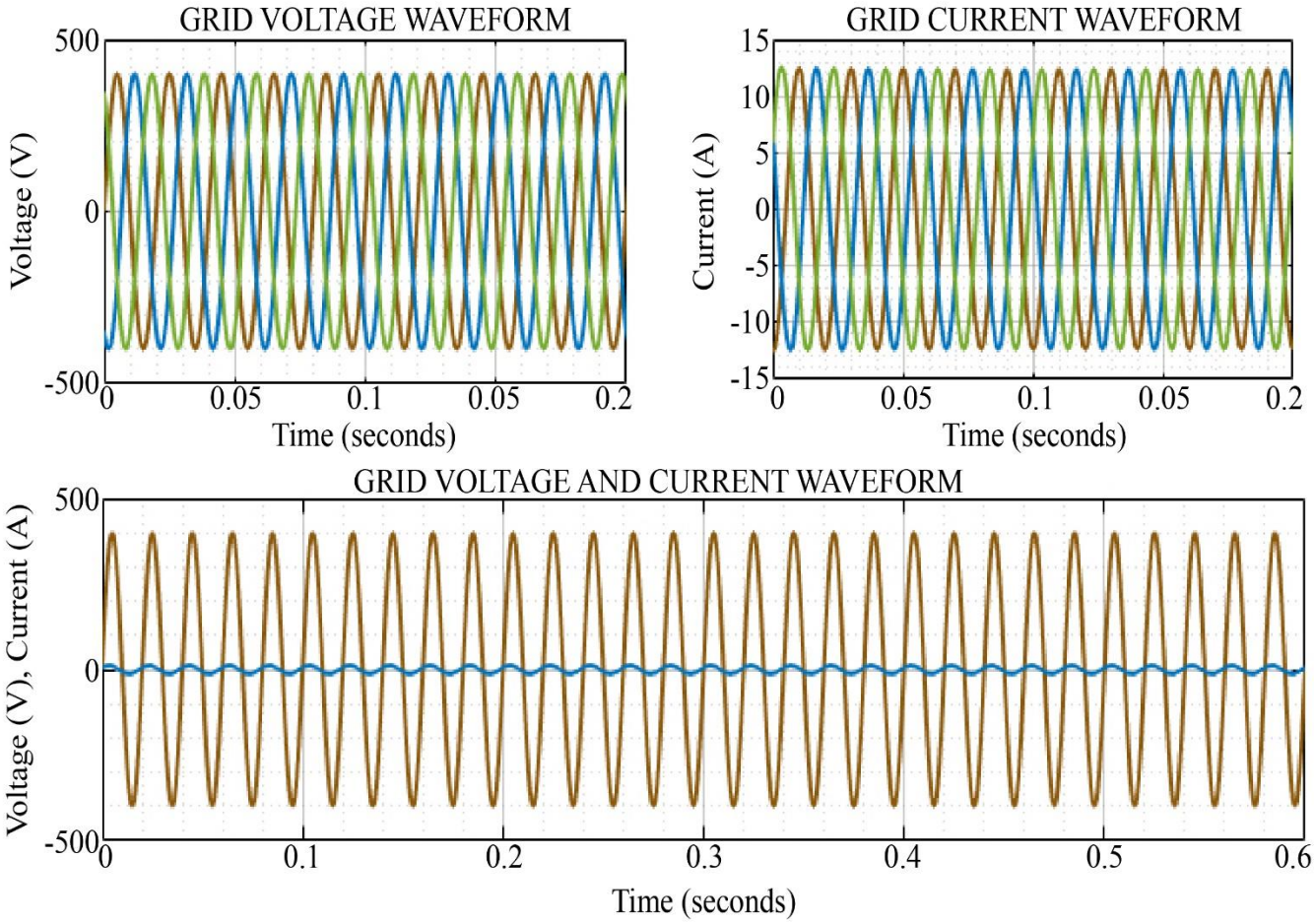

Fig. 21 Grid characteristics waveform

The harmonics analysis of three-phase grid current is represented in Figure 22, with respect to the THD values. It is noticed that the R-phase exhibits a THD of 0.65%, the Y-phase has a THD of 0.71%, and the B-phase shows the lowest THD at 0.48%. This indicates effective harmonic mitigation and compliance with grid standards.

The comparison graph in Figure 23 illustrates the efficiency of the proposed HGBZ converter against other high-gain converters. Proposed HGBZ achieves the highest efficiency of 95.33%, outperforming High Gain Boost [23] with 95% and High Gain Quadratic Boost of 92% [24]. The High Gain SEPIC [25] with 91.4% and High Gain Cuk [26] with 90% converters show lower efficiency, highlighting the superior performance of the HGBZ for energy conversion. Meanwhile, MPPT tracking efficiency of proposed ICO-ANN achieves the highest tracking efficiency of 98.99%, surpassing ABC [20] with98.92%, IGWO of [27] with 98.54%, and APO of [28] with 97.86%. The HPIO method [29] exhibits the lowest efficiency at 92.77%. This demonstrates the superior performance of the ICO-ANN algorithm in maximizing power extraction under varying solar conditions. This comparison demonstrates the proposed converter's suitability for efficient PV-based EV charging systems.

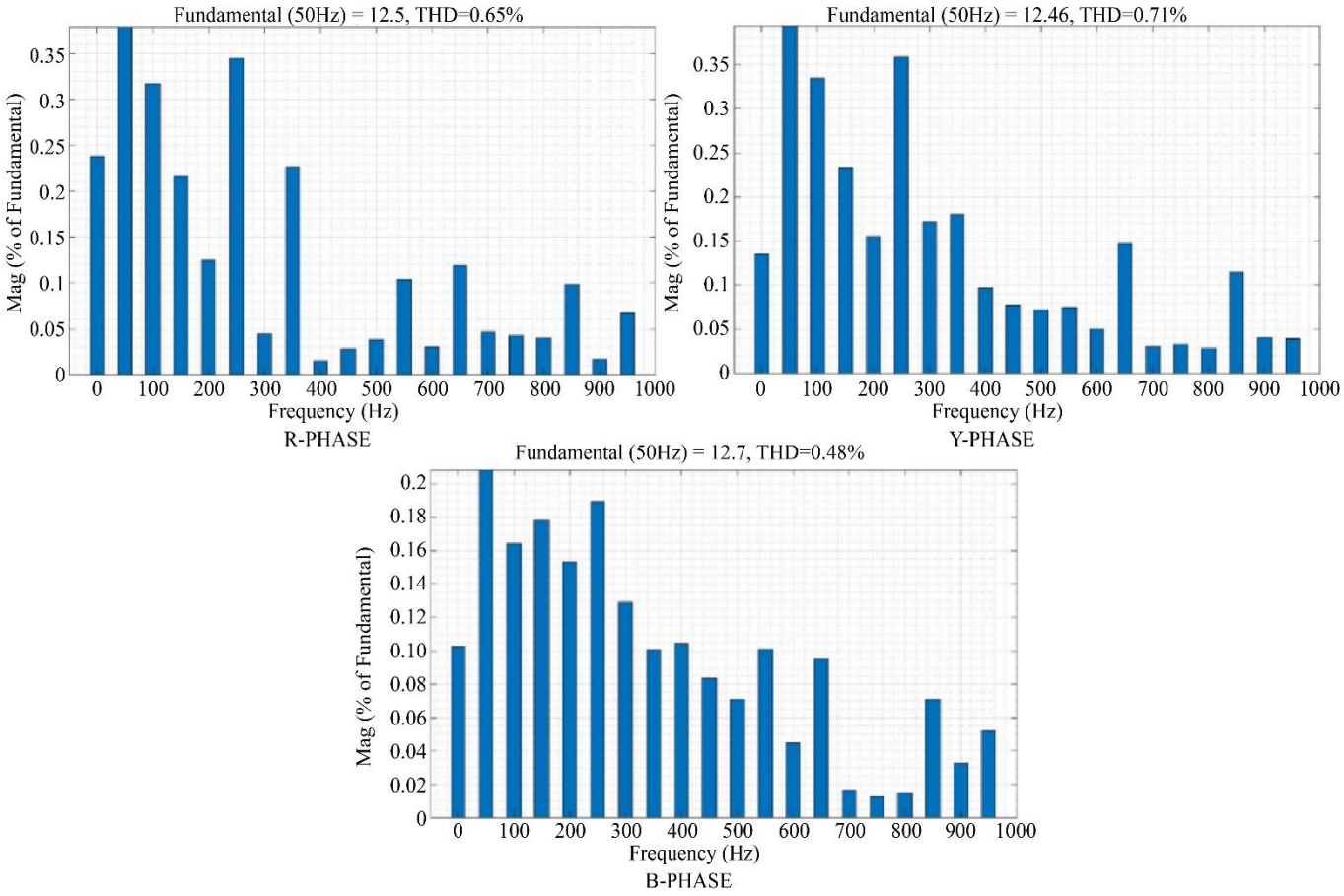

Fig. 22 Grid current THD waveform for RYB phase

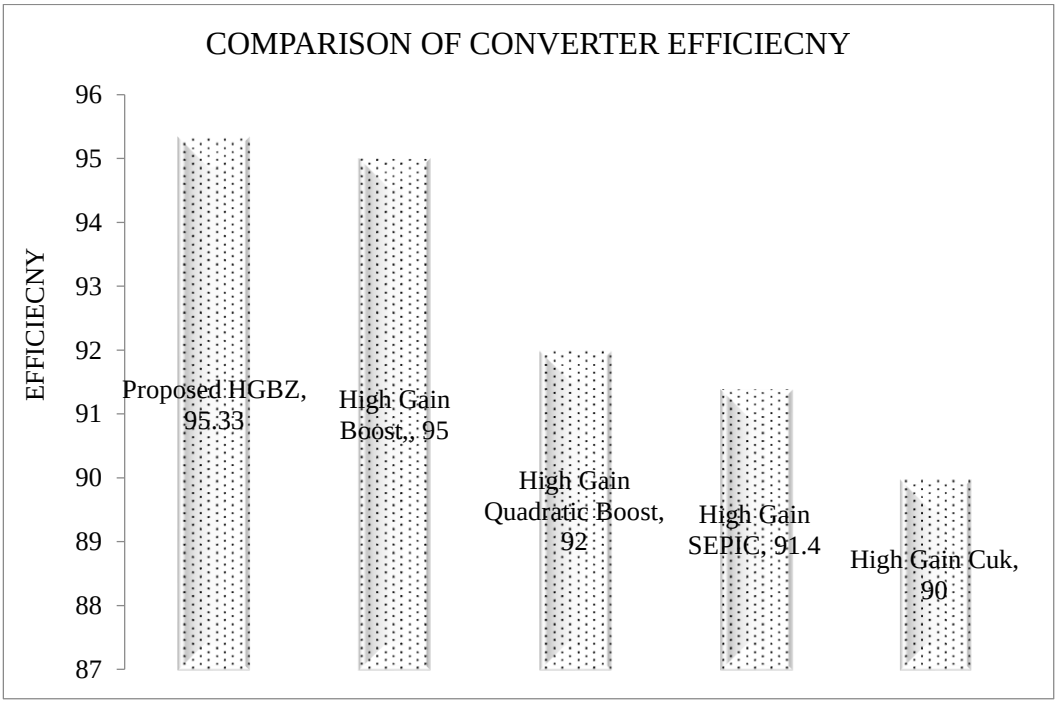

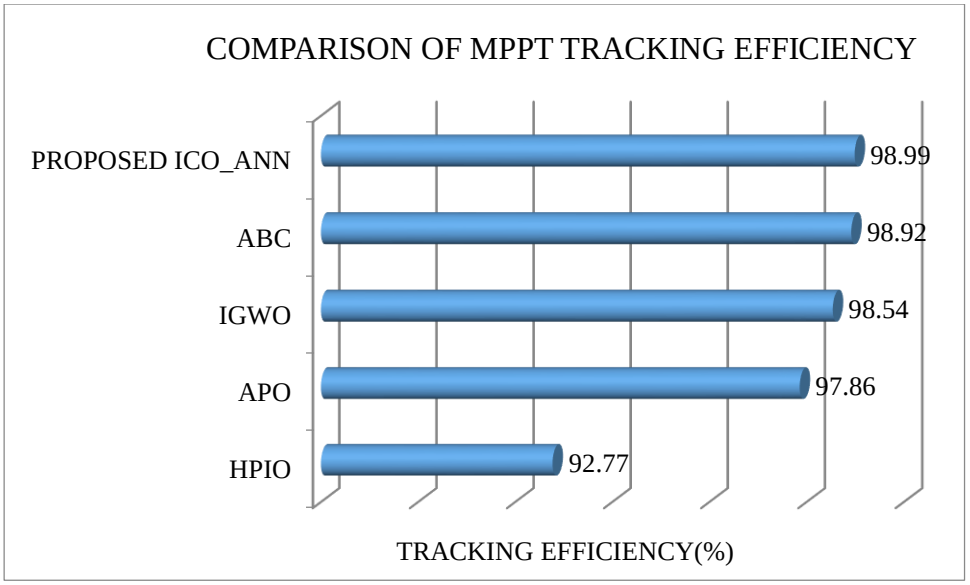

Fig. 23 Comparison of converter and MPPT tracking efficiency

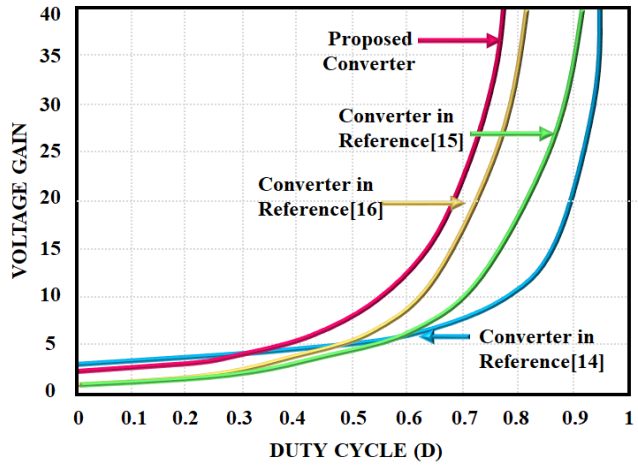

Fig. 24 Analysis of voltage gain

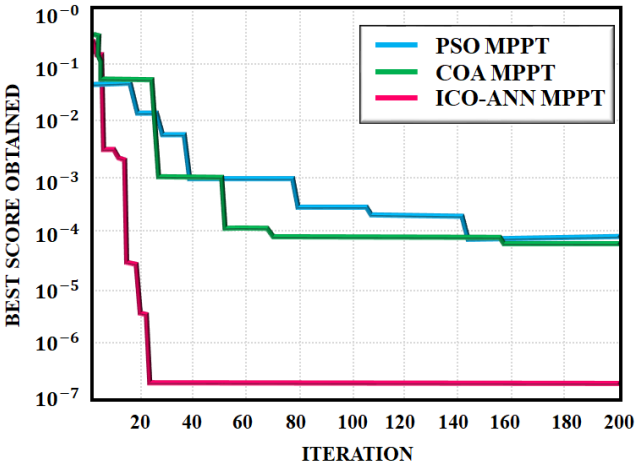

Fig. 25 Comparison of convergence curve

Comparison of the voltage gain of the proposed HGBZ converter with existing converters from references [11-13] over varying duty cycles is demonstrated in Figure 24. The proposed converter exhibits the highest voltage gain, demonstrating superior performance, especially at higher duty cycles. Converters from references [11-13] show comparatively lower voltage gain, indicating reduced efficiency in boosting voltage. This reveals the effectiveness of the proposed HGBZ converter in achieving higher voltage conversion for EV charging applications. This improved efficiency is attained by the careful selection of components and a refined control strategy.

Assessment of MPPT tracking approaches in terms of convergence is illustrated in Figure 25. It is worth noting that the ICO-ANN MPPT demonstrates the fastest and most precise convergence, reaching the lowest error value early. While the COA MPPT and PSO MPPT show slower convergence with higher residual error. This indicates that the ICO-ANN MPPT algorithm outperforms others in terms of tracking accuracy and efficiency. The hybrid algorithm performs the dynamic adjustment of parameters under varying conditions, leading to rapid adaptation and improved convergence.

5. Conclusion

This paper proposes a PV-based EV charging system demonstrating significant advancements in sustainable energy utilization, accomplishing high efficiency and reliability. The integration of the HGBZ converter ensures an efficient energy level boost suitable for charging EVs. The utilization of ICO-ANN MPPT supports the maximum power extraction from the PV array, enabling consistent and reliable energy generation under changing conditions. The bidirectional DC-DC converter linked to the battery system further enhances

flexibility by allowing excess solar energy to be stored for later usage, ensuring an uninterrupted power supply even during times of low generation of PV. Moreover, the integration of the grid enables surplus energy to be fed into the grid or additional power to be drawn as needed.

This bidirectional capability promotes efficient energy management and contributes to grid stability.MATLAB simulation results foreshow that the proposed converter outperforms with notable efficiency of 95.33%, with ICO-ANN MPPT ranking with exceptional tracking efficiency of 98.99% revealing superior performance compared to state-of-the-art methods. The system's high efficiency and innovative components demonstrate its potential to reduce grid dependency, lower carbon emissions, and provide a reliable and eco-friendly EV charging solution. Actually, computational complexity has to be considered due to the integration of ICO with ANN. In the future, this issue has to be considered, with a focus on reducing resource consumption and processing time.

References

[1] K.S. Kavin et al., "Improved BRBFNN-Based MPPT Algorithm for Coupled Inductor KSK Converter for Sustainable PV System Applications," *Electrical Engineering*, vol. 107, no. 6, pp. 7831-7853, 2025. [CrossRef] [Google Scholar] [Publisher Link]

[2] B. Siva Krishna, U. Lilli Kumar, and J. Vishwanath Rao, "Hybrid Renewable Energy Sources Based Active Power Filter with Predictive Fuzzy Controller to Improve Power Quality," 2015. [Google Scholar]

[3] Deepak Mohanraj et al., "Critical Aspects of Electric Motor Drive Controllers and Mitigation of Torque Ripple," *IEEE Access*, vol. 10, pp. 73635-73674, 2022. [CrossRef] [Google Scholar] [Publisher Link]

[4] M. Aishwarya, and R.M. Brisilla, "Design and Fault Diagnosis of Induction Motor using ML-Based Algorithms for EV Application," *IEEE Access*, vol. 11, pp. 34186-34197, 2023. [CrossRef] [Google Scholar] [Publisher Link]

[5] Qi Huang et al., "Design and Research of Permanent Magnet Synchronous Motor Controller for Electric Vehicle," *Energy Science & Engineering*, vol. 11, no. 1, pp. 112-126, 2023. [CrossRef] [Google Scholar] [Publisher Link]

[6] Mahesh A. Pate et al., "Design and Optimisation of Slotted Stator Tooth Switched Reluctance Motor for Torque Enhancement for Electric Vehicle Applications," *International Journal of Ambient Energy*, vol. 43, no. 1, pp. 4283-4288, 2022. [CrossRef] [Google Scholar] [Publisher Link]

[7] Hui Wang et al., "Design and Control of Wireless Permanent-Magnet Brushless Dc Motors," *IEEE Transactions on Energy Conversion*, vol. 38, no. 4, pp. 2969-2979, 2023. [CrossRef] [Google Scholar] [Publisher Link]

[8] Carlos Restrepo et al., "Improved Model Predictive Current Control of the Versatile Buck-Boost Converter for a Photovoltaic Application," *IEEE Transactions on Energy Conversion*, vol. 37, no. 3, pp. 1505-1519, 2022. [CrossRef] [Google Scholar] [Publisher Link]

[9] Yousef Alharbi, and Ahmed Darwish, "Control of Cuk-Based Microinverter Topology with Energy Storage for Residential PV Applications," *Energies*, vol. 16, no. 5, pp. 1-23, 2023. [CrossRef] [Google Scholar] [Publisher Link]

[10] Alakshyender Singh, Jitendra Gupta, and Bhim Singh, "Bridgeless Modified High-Step-Up Gain SEPIC PFC Converter-Based Charger for Light EVs Battery," *IEEE Transactions on Industry Applications*, vol. 59, no. 5, pp. 6155-6166, 2023. [CrossRef] [Google Scholar] [Publisher Link]

[11] M. Karthikeyan et al., "A Hybridization of Cuk and Boost Converter using Single Switch with Higher Voltage Gain Compatibility," *Energies*, vol. 13, no. 9, pp. 1-24, 2020. [CrossRef] [Google Scholar] [Publisher Link]

[12] Haris Ataullah et al., "High Gain Coupled Inductor SEPIC based Boost Inverter using Extended SPWM," *Energy Reports*, vol. 10, pp. 4013-4024, 2023. [CrossRef] [Google Scholar] [Publisher Link]

[13] Ramanathan Gopalasami, Bharatiraja Chokkalingam, and Suresh Muthusamy, "A Novel Method for Hybridization of Super Lift Luo Converter and Boost Converter for Electric Vehicle Charging Applications," *Energy Sources, Part A: Recovery, Utilization, and Environmental Effects*, vol. 45, no. 3, pp. 8419-8437, 2023. [CrossRef] [Google Scholar] [Publisher Link]

[14] Xibeng Zhang et al., "Hybrid Maximum Power Point Tracking Method based on Iterative Learning Control and Perturb & Observe Method," *IEEE Transactions on Sustainable Energy*, vol. 2, no. 1, pp. 659-670, 2020. [CrossRef] [Google Scholar] [Publisher Link]

[15] Mohammad Haziq Ibrahim et al., "Optimizing Step-Size of Perturb & Observe and Incremental Conductance MPPT Techniques Using PSO for Grid-Tied PV System," *IEEE Access*, vol. 11, pp. 13079-13090, 2023. [CrossRef] [Google Scholar] [Publisher Link]

[16] Bushra Sabir et al., "A Novel Isolated Intelligent Adjustable Buck-Boost Converter with Hill Climbing MPPT Algorithm for Solar Power Systems," *Processes*, vol. 11, no. 4, pp. 1-23, 2023. [CrossRef] [Google Scholar] [Publisher Link]

[17] Shaik Rafi Kiran et al., "Reduced Simulative Performance Analysis of Variable Step Size ANN-based MPPT Techniques for Partially Shaded Solar PV Systems," *IEEE Access*, vol. 10, pp. 48875-48889, 2023. [CrossRef] [Google Scholar] [Publisher Link]

[18] Aouatif Ibnelouad et al., "Improved Cooperative Artificial Neural Network-Particle Swarm Optimization Approach for Solar Photovoltaic Systems using Maximum Power Point Tracking," *International Transactions on Electrical Energy Systems*, vol. 30, no. 8, 2020. [CrossRef] [Google Scholar] [Publisher Link]

[19] Jesus Aguila-Leon et al., "Solar Photovoltaic Maximum Power Point Tracking Controller Optimization using Grey Wolf Optimizer: A Performance Comparison Between Bio-Inspired and Traditional Algorithms," *Expert Systems with Applications*, vol. 211, pp. 1-22, 2023. [CrossRef] [Google Scholar] [Publisher Link]

[20] Catalina González-Castaño et al., "MPPT Algorithm Based on Artificial Bee Colony for PV System," *IEEE Access*, vol. 9, pp. 43121-43133, 2021. [CrossRef] [Google Scholar] [Publisher Link]

[21] Nassir Deghfel et al., "A New Intelligently Optimized Model Reference Adaptive Controller using GA and WOA-based MPPT Techniques for Photovoltaic Systems," *Scientific Reports*, vol. 14, no. 1, pp. 1-21, 2024. [CrossRef] [Google Scholar] [Publisher Link]

[22] Abdulbari Talib Naser et al., "A Fast-Tracking MPPT-Based Modified Coot Optimization Algorithm for PV Systems under Partial Shading Conditions," *Ain Shams Engineering Journal*, vol. 15, no. 10, pp. 1-15, 2024. [CrossRef] [Google Scholar] [Publisher Link]

[23] Arshad Mahmood et al., "A Non-Inverting High Gain Dc-Dc Converter with Continuous Input Current," *IEEE Access*, vol. 9, pp. 54710-54721, 2021. [CrossRef] [Google Scholar] [Publisher Link]

[24] S.V.K. Naresh, Sankar Peddapati, and Mamdouh L. Alghaythi, "Non-Isolated High Gain Quadratic Boost Converter based on Inductor's Asymmetric Input Voltage," *IEEE Access*, vol. 9, pp. 162108-162121, 2021. [CrossRef] [Google Scholar] [Publisher Link]

[25] Pandav Kiran Maroti et al., "A New Structure of High Voltage Gain SEPIC Converter for Renewable Energy Applications," *IEEE Access*, vol. 7, pp. 89857-89868, 2019. [CrossRef] [Google Scholar] [Publisher Link]

[26] Zeeshan Haider et al., "Development and Analysis of a Novel High-Gain CUK Converter using Voltage-Multiplier Units," *Electronics*, vol. 11, no. 17, pp. 1-16, 2022. [CrossRef] [Google Scholar] [Publisher Link]

[27] Ke Guo et al., "An Improved Grey Wolf Optimizer MPPT Algorithm for PV System with BFBIC Converter under Partial Shading," *IEEE Access*, vol. 8, pp. 103476-103490, 2020. [CrossRef] [Google Scholar] [Publisher Link]

[28] Akhil Raj, and R.P. Praveen, "Highly Efficient DC-DC Boost Converter Implemented with Improved MPPT Algorithm for Utility Level Photovoltaic Applications," *Ain Shams Engineering Journal*, vol. 13, no. 3, pp. 1-9, 2022. [CrossRef] [Google Scholar] [Publisher Link]

[29] Zhuoli Zhao et al., "Hierarchical Pigeon-Inspired Optimization-Based MPPT Method for Photovoltaic Systems under Complex Partial Shading Conditions," *IEEE Transactions on Industrial Electronics*, vol. 69, no. 10, pp. 10129-10143, 2021. [CrossRef] [Google Scholar] [Publisher Link]